Melt electrowritten scaffolds containing fluorescent nanodiamonds for improved mechanical properties and degradation monitoring

Wu, Xixi; Vedelaar, Thea; Li, Runrun; Schirhagl, Romana; Kamperman, Marleen; Włodarczyk-Biegun, Małgorzata K.

Published in:
Bioprinting

DOI:
10.1016/j.bprint.2023.e00288

Bioprinting 32 (2023) e00288

Contents lists available at ScienceDirect

Bioprinting

journal homepage: www.sciencedirect.com/journal/bioprinting

Melt electrowritten scaffolds containing fluorescent nanodiamonds for improved mechanical properties and degradation monitoring

Xixi Wu [a], Thea Vedelaar [a], Runrun Li [a], Romana Schirhagl [a], Marleen Kamperman [b], Małgorzata K. Włodarczyk-Biegun [a,b,c,*]

[a] Department of Biomedical Engineering, University Medical Centre Groningen and University of Groningen, Ant. Deusinglaan 1, 9713, AV, Groningen, the Netherlands
[b] Polymer Science, Zernike Institute for Advanced Materials, University of Groningen, Nijenborgh 4, Polymer Science, 9747, AG, the Netherlands
[c] Biotechnology Centre, The Silesian University of Technology, Krzywoustego 8, 44-100, Gliwice, Poland

ARTICLE INFO

Keywords:
Fluorescent nanodiamonds
Degradation detection
NV centers
Melt electrowriting
Scaffolds

ABSTRACT

Biocompatible fluorescent nanodiamonds (FNDs) were introduced into polycaprolactone (PCL) – the golden standard material in melt electrowriting (MEW). MEW is an advanced additive manufacturing technique capable of depositing high-resolution micrometric fibres. Due to the high printing precision, MEW finds growing interest in tissue engineering applications. Here, we introduced fluorescent nanodiamonds (FNDs) into polycaprolactone prior to printing to fabricate scaffolds for biomedical applications with improved mechanical properties. Further FNDs offer the possibility of their real-time degradation tracking. Compared to pure PCL scaffolds, the functionalized ones containing 0.001 wt% of 70 nm-diameter nanodiamonds (PCL-FNDs) showed increased tensile moduli (1.25 fold) and improved cell proliferation during 7-day cell cultures (2.00 fold increase). Furthermore, the addition of FNDs slowed down the hydrolytic degradation process of the scaffolds, accelerated for the purpose of the study by addition of the enzyme lipase to deionized water. Pure PCL scaffolds showed obvious signs of degradation after 3 h, not observed for PCL-FNDs scaffolds during this time. Additionally, due to the nitrogen-vacancy (NV) centers present on the FNDs, we were able to track their amount and location in real-time in printed fibres using confocal microscopy. This research shows the possibility for high-resolution life-tracking of MEW PCL scaffolds' degradation.

1. Introduction

Tissue scaffolds which mimic different aspects of extracellular matrix (ECM) play a very important role in modulating cell performance to create a certain tissue environment [1–3]. Scaffold architecture, mechanical properties (e.g. modulus) and defined porosity can significantly influence the functionality of the artificial tissue [4–6]. Melt electrowriting (MEW), a 3D printing method utilizing molten thermoplastic materials in the presence of an electrical field, allows to obtain well-defined scaffolds with an unprecedented precision. Benefited by the easy-operation and environmentally-friendly features, MEW is an effective method to design and manufacture scaffolds [7–9] with high flexibility in the designs, and bio-instructive properties.

PCL is approved by the food and drug administration (FDA) and the gold standard material for MEW due to its easy processability and good printability. PCL scaffolds with different structures were printed with MEW to observe cell growth direction [8,10] and cell-specific bridging behaviour [11] scaffolds for skin [12], osteochondral [13] tissue engineering and heart patches [14]. To modify the properties of PCL and modulate its degradation rate [15–17], decrease its hydrophobicity [18] and improve mechanical properties [19] fillers as graphene [17], calcium phosphate [20,21] or nanodiamonds [22,23] were used in different fabrication approaches. However, till now, for MEW only PCL modified with graphene [17], hydroxyapatite [24] and milk protein [25] was used. In the first study, it was shown that the tensile strength of the PCL/graphene scaffold (with 0.5 wt% graphene) was improved significantly (by more than 270%) compared to pristine PCL scaffold. Furthermore, enzymatic degradation was slowed down by adding graphene (0.1, 0.5 wt%) into the PCL material [17]. In the second study, near-field direct-writing melt electrospinning was used to gain nano-hydroxyapatite PCL/nHA composite scaffolds with excellent mechanical properties and desired morphology. Further, ceramic biomaterial for osteogenic properties were introduced in bone tissue

* Corresponding author. Polymer Science, Zernike Institute for Advanced Materials, University of Groningen, Nijenborgh 4, Polymer Science, 9747, AG, the Netherlands
E-mail addresses: m.k.wlodarczyk@rug.nl, malgorzata.wlodarczyk-biegun@polsl.pl (M.K. Włodarczyk-Biegun).

https://doi.org/10.1016/j.bprint.2023.e00288
Received 13 January 2023; Received in revised form 31 May 2023; Accepted 1 June 2023
Available online 2 June 2023

Abbreviations

PCL:	polycaprolactone
FND	fluorescent nanodiamonds
MEW	melt electrowriting
NV	nitrogen-vacancy
MPs	milk proteins
LF	lactoferrin
WP	whey protein
NDs	nanodiamonds
NHDF-Ad cells	Normal Adult Human Dermal Fibroblast cell
%ABr	Absolute % AlamarBlue reduction
DMEM	Dulbecco's Modified Eagle Medium
ANOVA	one-way analysis of variance
HSD	Tukey's honestly significant difference post hoc test
IQR	interquartile range

engineering [24]. In the third study, bioactive milk proteins (MPs), lactoferrin (LF) and whey protein (WP) at varying concentrations (0.05%, 0.1%, 0.25%) were blended with PCL to promote skin regeneration using MEW. The combined addition of LF and WP increased the biological activity, cell growth, spreading, and infiltration, of MEW PCL scaffolds [25].

Nanodiamonds, which have shown to be biocompatible [26,27], have been investigated for its distinct chemical [28], physical [29,30] and quantum properties [31–33]. Multifunctional composites containing nanodiamonds can enhance polymeric properties including hydrophilicity, stability as well as influence cell behaviour like cell adhesion and proliferation when imbedded in biopolymers [34–38]. Due to the presence of negatively charged nitrogen-vacancy (NV) centers they are fluorescent and can be used to sense physical parameters including magnetic and electric fields and temperature under ambient magnetic and temperature conditions [33,34]. Additionally, intracellular free radicals can be detected via the NV-centre quantum sensing [39], which can be used to test the amount of free radicals and effect of antioxidants employed in biomedical research. Based on these features, nanodiamonds allow detecting biomedical information [40,41] such as subcellular thermal changes and intracellular temperature changes. Therefore, they are attractive fillers for use in biomedical applications.

Recently, it was reported that scaffolds obtained from PCL combined with nanodiamonds, using electrospinning, displayed an increased tensile modulus and improved cell viability, proliferation rate and cell adhesive behaviour [27,28,32]. Particularly, Guk Young Ahn [33] prepared PCL/ND materials using NDs with a positive charge (46.0 ± 3.4 mV) and found the electrospun PCL/ND fibrous matrix with 1 wt% of NDs had the highest tensile strength among the tested samples (0.5 wt% to 3 wt%). This material was also characterized by improved proliferation and differentiation of MC3T3-E1 cells. Shadi Houshyar et al. [17] introduced detonation NDs into PCL and electrospun nanodiamond/poly-ε-caprolactone nanofibrous scaffold for wound management. The authors showed that the scaffold potentially provides essential properties for wound healing by enhancing proliferation of epithelial cells, in addition to restricting the microbial activities.

Herein, we fabricate PCL-FNDs scaffolds at a micrometre scale using melt electrowriting (MEW) (Fig. 1a). We show for the first time that the magnetooptical properties of FNDs can be used to monitor the degradation process of printed scaffolds on the single particle level (Fig. 1b). To achieve this goal, we used T1 relaxation measurements which are equivalent to T1 in conventional magnetic resonance imaging (MRI) but from a nanoscale environment [42–44]. Such measurements allow quantification of free radicals via their free electron spin in living cells. To this end, we used a series of FND concentrations (0–0.1 wt%) well-dissolved in PCL to produce well-defined scaffolds for Normal Adult Human Dermal Fibroblast cell culture using MEW (Fig. 1a). Rising FND concentrations in PCL did not compromise the mechanical properties in comparison with control PCL films. Based on the optimal Young's modulus and the possibility of fluorescence-based tracking, 0.001 wt% was selected for PCL-FNDs blends for further degradation and cell behaviour research. The degradation studies show that fibres containing FNDs degraded slowly within 1 week of enzyme treatment in comparison to fibres printed with pure PCL. T1 relaxation time measurements were performed in order to confirm the degradation profile of the scaffolds. Cell studies revealed that PCL-FNDs scaffolds were biocompatible evaluated by high cell viability and better cell proliferation behaviour compared to pure PCL scaffolds.

2. Materials and methods

2.1. Preparation of PCL-FND mixture

2 g medical grade polycaprolactone pellets (PCL, Purasorb PC 12, Corbion) were dissolved in 30 mL 1,1,1,3,3,3-hexafluoro-2-propanol (HFP, Bioslove). Fluorescent nanodiamonds (FNDs, Adamasnano) with a hydrodynamic diameter of 70 nm were used. They were produced by the manufacturer as follows [45]. First diamonds were produced by high pressure high temperature synthesis followed by irradiation (with an electron beam at 3 MeV and a fluence of 5 x 10^{19} e/cm^2) and annealing above 600 °C. As a result of this process each particle contained around 500 nitrogen vacancy centers which fluoresce in a broad peak above 600 nm. As a last step of their synthesis, they were treated with oxidizing acids resulting in an oxygen terminated surface. These particles have been extensively used and characterized in earlier literature [46]. 2 mg/ml fluorescent nanodiamonds were dispersed in deionized water and mixed with PCL solution to get PCL-FND mixtures. The mixtures were heated up to 50 °C and stirred at 1000 rpm for 30 min in order to prepare a homogeneous solution. The solvents were dried as descripted in the following paragraph.

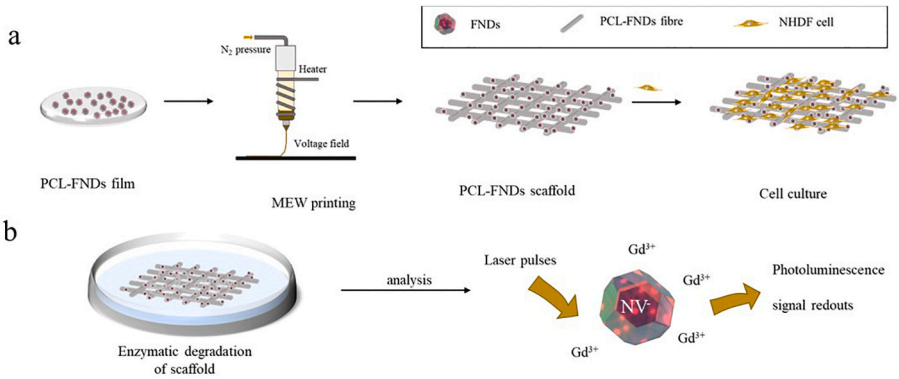

Fig. 1. Overview of PCL-FNDs mesh printing and cell behaviour and enzymatic degradation research on the meshes. a) Preparation of MEW PCL-FNDs meshes. FNDs were well dispersed in PCL material, films of composites were cut into pieces and heated in a steel cartridge and printed using MEW. The cytocompatibility was also tested using normal human dermal fibroblasts (NHDF-Ad). b) Enzymatic degradation and following detection of meshes. The meshes were immersed inside the enzyme solution and degraded up to 7 days, the PCL-FNDs meshes containing nanodiamond sensors was immersed in Gd^{3+} in aqueous solution, when meshes were degraded, Gd^{3+} can come closer to FNDs, thus the relaxation time decreases which was captured by a home-made magnetometry setup.

2.2. Physical properties of the films

PCL and PCL-FND films were used as reference materials. The films were prepared as follows: PCL-FND films were obtained by casting the mixture onto glass dishes and evaporating HFP slowly at 60 °C for 1 h. The final FND concentrations were 0.001, 0.005, 0.01, 0.1 wt%. Pristine PCL without nanodiamonds was used as a control printable material. Prior to printing, the films were loaded into the heated cartridge and melted for 30 min, as describe below in section 2.3.

2.2.1. Mechanical testing

Young's moduli of PCL and PCL-FNDs rectangular films were analysed using an Instron 5565 100 N Series IX tensile tester with a 0.1 kN load cell. Sample thicknesses of each experimental group were measured using an electrical calliper and after each measurement, the dimensions of films were confirmed: 20 mm × 10 mm x 0.1 mm, the testing gauge was kept at 5 mm with the elongation speed at 10 mm/min.

Based on tensile testing, 0.001 wt% FND-doping concentration resulted in the highest tensile modulus and therefore was selected for the rest of the experiments.

2.2.2. Crystallization analysis and thermal stability

Crystallinity of pure PCL and nanodiamond imbedded film (0.001 wt %) were measured using a differential scanning calorimeter (DSC, PerkinElmer DSC-7) from −40 °C to 140 °C in N_2 atmosphere. Specimens of 3–6 mg were precisely weighed by Quintix® Semi-Micro Balances and sealed in aluminium pans for the measurement, then heated to 140 °C from the settled temperature. This was followed by cooling to −40 °C and reheating up to 140 °C with a scanning speed at 10 °C/min, melting behaviour and crystallinity were evaluated. The degree of crystallinity (*Xc*) for each sample was calculated by the following equation [47]:

$$Xc(\%) = \frac{\Delta Hsamples}{\varphi \Delta H0}$$

where.

$\Delta H_{samples}$ refers to the melting enthalpy integrated from the second heating curves, φ is the weight percentage of PCL in this composite, ΔH_0 is the standard fusion enthalpy for 100% crystalline PCL, with a value of 142 J/g [48].

Thermal stability of the PCL and FNDs-modified materials were characterized by using thermogravimetry (TGA). Specimens were prepared as follows. 3–6 mg were weighed accurately by a PerkinElmer TGA-7 machine. The scanning temperature range of was 0–700 °C under nitrogen flow at 10 °C/min.

2.3. Fabrication of PCL and PCL-FND meshes

Films were cut into pieces and melted in a stainless-steel syringe cartridge at 100 °C for 30 min and then meshes with a strand spacing of 250 μm were printed with a melt electrowriting machine (Spraybase® A-1204-0001-01D, Ireland) [49]. Briefly, 8 layers of square designs with 230 μm inter-fiber distance leading to final scaffold dimensions of 15 mm × 15 mm x 0.08 mm were printed using 0.15–0.17 bar air pressure through a 0.35 mm nozzle (E3D online, UK). A high voltage of 6 kV was used, and fibres were deposited directly on the aluminium collector. The height between the needle and collector was kept at 4 mm and the collecting velocity was 250 mm/min. An electricity release gun and mat were used to remove the charges on the scaffolds.

2.4. Characterization of printed meshes

2.4.1. Morphology tests using SEM

Morphology images from the top view and 30° rotation angle were obtained using a field emission scanning electron microscope (FEI Nova NanoSEM 650 scanning electron microscope, the USA). The polymer specimens were coated with gold plasma at 15 nm-thickness and investigated under an electron beam with a voltage of 15 kV.

2.4.2. Mechanical testing

Young's moduli of PCL-FND square meshes were analysed using the same procedure as we mentioned in 2.2.1. The dimensions of fibrous square patterns were: 15 mm × 15 mm x 0.08 mm.

2.5. Enzymatic degradation

It takes ca. 2 years for PCL to degrade completely in vivo and in vitro [50]. To facilitate and observe the degradation process, 3 samples of pristine PCL and PCL fibrous meshes with 0.001% FNDs were used. Meshes at 2.5 mg were submerged in 2 mL of 2 mg/mL lipase, which is extracted from pseudomonas cepacian pow (PS Lipase, Sigma). Samples were put into 24-well plates at room temperature. After certain time intervals (3 h, 8 h, 1 day, 3 days, 7 days), the enzymatic solution was removed and degraded samples were rinsed 3 times with de-ionized water. At last, to fasten the drying process, the specimens were immersed with 96% ethanol and then the ethanol was removed and the samples were dried for 2 days at room temperature. Crystallinity of these degraded samples were measured following the protocol described in 2.2.2. Surface wettability before and after degradation were analysed using contact angle goniometry on a Data Physics OCA30, USA. 5 measurements were performed on each sample and the average of those values was reported. Images were taken from the Dataphysics OCA30 setup software. Fibre diameters were calculated using ImageJ (National Institutes of Health software), 20 fibres were measured per sample and 3 samples were used for each group, average values were obtained.

2.6. Fluorescent imaging and T1 measurements

Relaxometry measurements allow to determine the concentration of paramagnetic species in the surrounding. This is done by pumping NV centers in the bright ms = 0 state of the ground state. After different dark times we probed again if the NV centers have remained in the bright state or returned to the darker equilibrium between ms = 0 and ms = ±1. The relaxometry data is equivalent to T1 in conventional MRI but from nanoscale voxels. In presence of paramagnetic ions, this process occurs faster. To conduct the measurements fibrous matrices which were exposed to enzymes for 0 h, 1 day, 3 days and 7 days were introduced to a homemade magnetometer which was described earlier [51]. Then FNDs with 8 x 10^5–3 x 10^6 counts per second within the fibres were localized and selected for measurements. Particles with much smaller counts give more noisy data and if a particle has too many counts, it is likely a large aggregate. Once a good particle was identified we started T1 tests. We used the data processing routines described by Perona Martínez et al. [52,53]. To determine T1, we used 40 pulses and the dark times between 0.1 and 1000 μs were used. We measured 10 particles for every experimental group and each sample was tested in Milli-Q water. In order to use this method to assess degradation, it is required to add gadolinium to the pre-degraded samples. If the fibre was degraded, the FNDs are exposed to Gd3+ and the relaxation time is shortened [54]. 10 μM gadolinium in aqueous solution was used which was added in sequence. Extreme values determined by interquartile range (IQR) were excluded before averaging the resulting T1 values. The T1 relaxation curve was fitted with a biexponential function, and the longer-time component was reported as the T1 constant [55].

2.7. Cell behaviour on the printed scaffolds

8-layer scaffolds with a squared shape composed of pure PCL and PCL with 0.001 wt% FNDs were prepared for cell culture. Prior to cell seeding, printed samples were sterilised using UV irradiation for 30 min.

Then, the samples were immersed in 70% ethanol for 20 min and washed 3 times with phosphate-buffered saline (PBS, Sigma). NHDF-Ad cells (Lonza, The Netherlands) were used to test biocompatibility of the scaffolds. 1 mL of cell suspension was distributed at a density of 5 x 10^6 cells/mL onto each 15 mm × 15 mm mesh and cultures in DMEM medium containing 10% FBS and 1% penicillin-streptomycin. The cell-seeded meshes were transferred into a fresh 24-well plate after 1-day cell adhesion in order to remove noise from cells on the bottom of plates. Then cells were cultured at 37 °C, 5% CO_2 atmosphere for 7 days.

At day 3 and day 7 cell viability and metabolic activity were measured using Fluorescein Diacetate/Propidium Iodide (FDA/PI, Sigma) and AlamarBlue reagent (Thermo Fisher Scientific Inc. USA), respectively. In short, for a life/dead assay, cell culture medium was removed and samples were washed 3 times using PBS. Cells on a glass slide and after 70% ethanol treatment were used as positive and negative control, respectively. 200 µL PBS solution containing 6 µg/mL FDA and 20 µg/mL PI were added to the wells and incubated for 15 min at room temperature. After staining reagent aspiration and washing, the stained specimens were imaged using a confocal microscope (Zeiss LSM 710, Germany).

For metabolic activity tests, 20 µL of AlamarBlue, were added to each well containing the sample in 180 µL of fresh culture medium. Wells containing 180 µL medium without cells and 20 µL AlamarBlue were used as negative control. 20 µL of fully reduced AlamarBlue prepared by 20-min autoclaving were taken as positive control. After 3-h of incubation, the solution from samples and controls were extracted and transferred into 96-well plates. Relative fluorescence units (RFU) were measured by a microplate Fluorometer (Thermo scientific Fluoroskan, Netherlands) using 530 nm excitation and 590 nm emission wavelengths. Absolute % AlamarBlue reduction (%ABr) could be calculated by the following equation:

$$\%ABr = \frac{RFU_{samples} - RFU_N}{RFU_P - RFU_N}$$

where $RFU_{samples}$ means RFU irradiated from samples, RFU_N and RFU_P refers to fluorescent data that was obtained from negative and positive controls [56].

To get further information on cell spreading, at day 3 and 7, the cytoskeleton was visualized using F-actin staining with Phalloidin-iFluor 488 reagent (Abcam), and cell nuclei with 4′,6-diamidino-2-phenylindole (DAPI, Sigma). In brief, cells on the meshes and glass slides (control group) were first fixed with 4% paraformaldehyde (PFA, Sigma) for 10 min, then samples were rinsed 3 times with PBS and permeabilized using 0.5% v/v Triton X-100 (Thermo Fisher) for 10 min. After washing 3 times with PBS, 200 µL F-actin staining solution (1 µg/mL in PBS with 1% BSA addition (Sigma)) was introduced to the samples for 30 min. Then the unbound phalloidin reagent was removed and the samples were rinsed 3 times (5 min each washing step). This step was followed by nucleus staining. To this end, 200 µL DAPI (5 µg/mL) were added to each well for 10 min, and cells were washed with PBS 3 times (5 min in each washing step). The cells and scaffolds were imaged with the same confocal microscope that was mentioned before.

2.8. Statistical analysis

All experimental results are reported as means ± standard deviation (s.d.). Statistical analysis was carried out by analysis of one-way variance (ANOVA) and Tukey's honestly significant difference (HSD) post hoc test. Data analysis was performed using GraphPad Prism software (GraphPad Software Inc., USA). Here * indicates $p < 0.05$, ** means $p < 0.01$, *** means $p < 0.001$ and **** means $p < 0.0001$.

3. Results and discussion

Fluorescent nanodiamonds were mixed into PCL and successfully printed using MEW. The thermal properties of the obtained printable material, printed scaffolds mechanical, and biological properties were tested and degradation monitored, as described below.

3.1. Crystallization analysis and thermal stability

PCL with nanodiamonds has a higher cooling temperature and crystallinity compared to PCL itself (Fig. 2a and b). The nanodiamonds can act as nucleating agents during PCL cooling. We expect that the crystallization of the material was facilitated with the help of FNDs [57] which was confirmed by the increased crystalline temperature upon cooling (Fig. 2a). Crystallinity of untreated PCL and PCL-FNDs meshes calculated here showed a slight increase (2%) when FNDs were introduced into PCL.

3.2. Morphology of scaffolds

Fig. 3 shows SEM images of well-aligned pure PCL and PCL-FNDs square matrices with gradually increasing concentrations of FNDs, observed from the bottom, the detaching layer. The printing pressure was adjusted to keep the fibre sizes at 20 ± 1.5 µm (from 0.15 to 0.17 bar), in all samples with and without FNDs in the printable material. This is important because fibre scaffolds were designed for versatile tissue engineering application with a 230 µm pore size and a 90% porosity approximately [58,59]. It is hard to print uniform PCL-FNDs patterns at higher resolution when concentration of FND goes over 0.01 wt% (fibre distance below 200 µm) because of the disturbance on the original PCL homogeneity and static electrical repulsion resulted from the employment of FNDs. When seeded on square scaffolds with 100, 200, 400 µm pore size, fibroblasts showed enhanced proliferation rate for pores bigger than >100 µm [60]. To get further detailed information about these scaffolds' printability, single.

fibres and fibre alignments in vertical direction were observed as well at high magnification. The fibres that contained FNDs were clearly rougher than the control fibres (see Fig. 3. Fibre surface). It is also salient that the fibre gap increased in the vertical direction (see Fig. 3. Lateral view-z axis indicated by arrows) as the amount of FNDs raised, whereas the fibre distance kept almost the same in horizontal direction (x, y axis). The higher cooling point of PCL-FNDs blend compared to PCL was one reason for the hanging of the fibres between the fibres (see Fig. 3 Lateral view). Certain residual charges are retained in deposited fibres during the printing process since the polymer is an electret in essence [61,62]. Nanodiamonds have higher polarity, caused by the presence of –COOH groups, than pure PCL. PCL has –COO groups according to the effective dipole moment theory [63]. Furthermore, FNDs used here have negatively charged nitrogen-vacancy centers and have a negative zeta potential. As a result, the mixture of FNDs in pristine PCL may carry more negative charges [64]. As reported by Kai Cao et al., when the layer number is small (we have printed only 8 layers), the deposited fibers are very likely to be negatively charged due to the rapid dissipation of positive charges [62]. The inflight fibre coming from the nozzle is positively charged and therefore can be attracted by the negatively charged bottom fibres and printing stage. Electrostatic attraction between adjacent fibres caused by those residual charges could be observed as sagging fibres (scaffolds were turned over when collecting them from the printing stage,- reverse visualization under SEM) and the extrusion segments evolved into an electrically-driven whipping instability circled in Fig. 3 top view [65–67]. Observed by SEM, 0.005 wt% PCL-FNDs meshes showed relatively bigger inter-fibre distance perpendicularly (10.5 ± 5.3 µm) than 0.01 wt% (7.7 ± 4.5 µm) and 0.1 wt% (6.9 ± 2.6 µm) samples, whereas fibre-fibre distance of pure PCL and 0.001 wt% PCL-FNDs matrix were 1.3 ± 0.3 µm. The planar alignment was affected slightly when the prescribed inter-fibre space was wide enough to avoid electrostatic interaction.

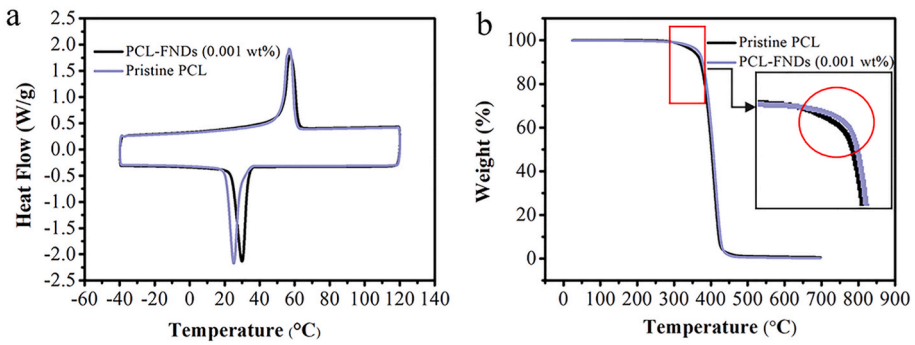

Fig. 2. Evaluation of the thermal stability of PCL and PCL-FNDs (0.001 wt%) materials a) Cooling and second heating curve of DSC. b) TGA profile showing the weight loss as a function of temperature.

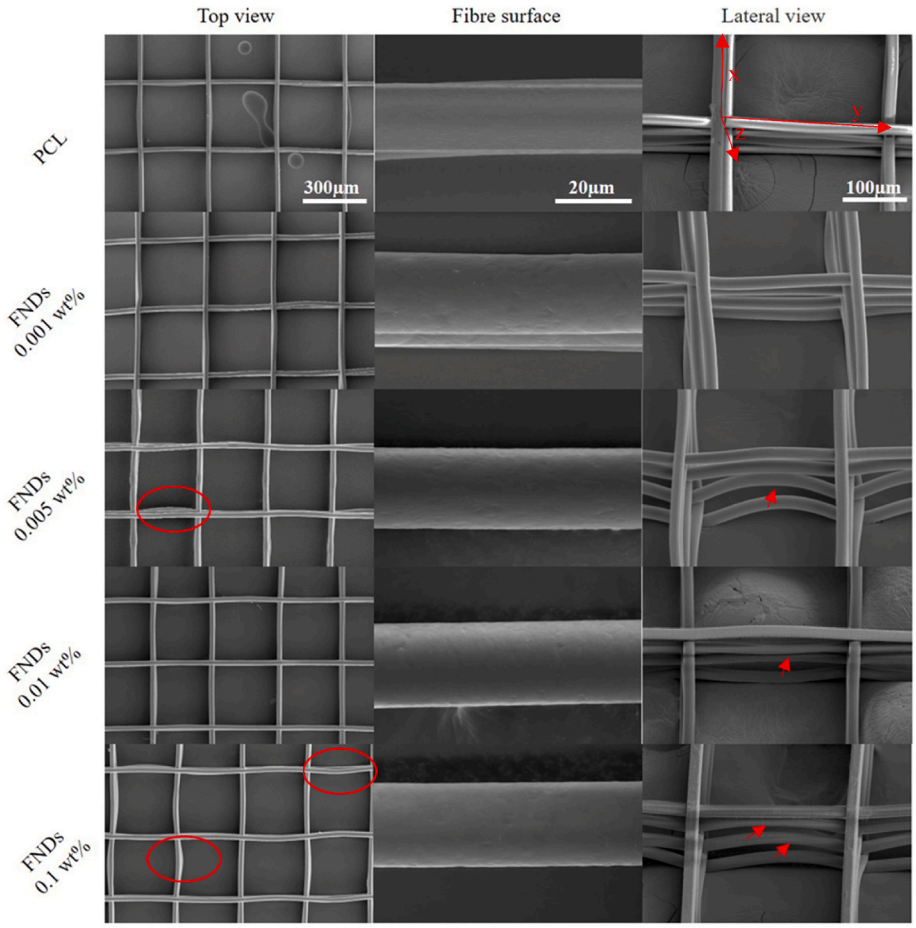

Fig. 3. SEM images of PCL and PCL-FND meshes containing different FND concentrations (as marked on the figure) printed by MEW: top view (scale bar 300 µm), magnified fibre surface (scale bar 20 µm), and lateral view (scale bar 100 µm). Red arrows are pointing at relatively large fibre distances in vertical direction (z-axis). (For interpretation of the references to colour in this figure legend, the reader is referred to the Web version of this article.)

3.3. Mechanical properties

The Young's moduli in tensile mode were measured to assess the mechanical properties of the scaffolds printed using PCL with different FND concentrations. As visible in Fig. 4b stiffness of the printed fibres increased after imbedding 0.001 wt% of FNDs into the PCL matrix, but decreased when higher concentrations of FNDs were used. For all tested scaffolds (Fig. 4c), the moduli significantly increased only for 0.001 wt %, all the other scaffolds did not reveal statistically significant differences.

Furthermore, the mechanical properties indicated that the MEW PCL scaffolds with 0.001 wt % FNDs have an obvious increase on the ultimate tensile strength (UTS), material with 0.1 wt% FNDs showed lowest maximum elongation. The other groups were analysed similarly (shown in SI Fig.S1). For bulk materials, no significant difference was observed on UTS or maximum elongation. Similar effects were recently reported for ND/poly (vinyl alcohol) composites [68] where the highest increase in Young's modulus and hardness occurred at very low concentrations of NDs (below 0.2 wt%). The authors attributed this increase to the uniform distribution of nanodiamonds. When the NDs are distributed uniformly with no agglomeration at a low concentration, this amplifies the strong interaction with the polymer molecules via elastic mechanism

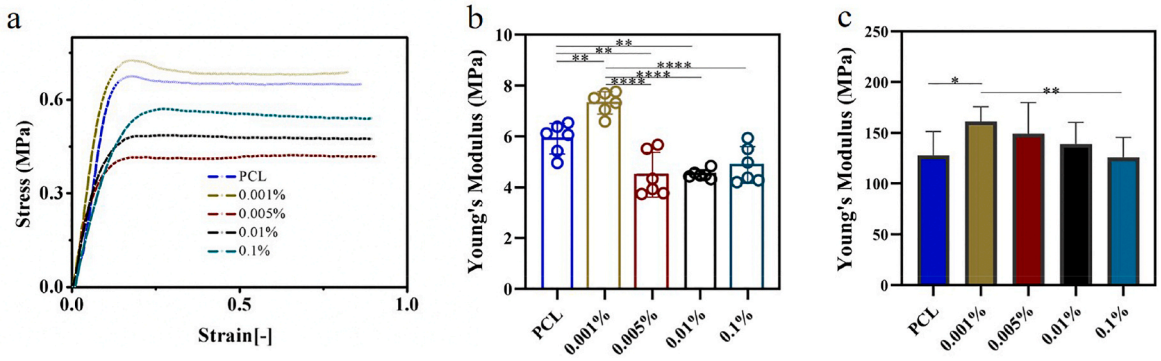

Fig. 4. Meshes and film mechanical properties of PCL-FND scaffolds with different FND concentrations (0, 0.001, 0.005, 0.01, 0.1 wt%). a) Representative fibrous matrix tensile stress-strain curves. b) Tensile Young's modulus of scaffolds. c) Tensile Young's modulus of films.

and plastic deformation features of the polymer.

The compared scaffolds had the same dimensions: shape with the same fibre size and inter-fiber distance, therefore their mechanical properties could be directly compared. Combining results of bulk mechanical properties of pure PCL and PCL-FNDs composite (Fig. 4c).

It can be concluded that the moduli of PCL were modified by mixing different amounts of FNDs into PCL. The aggregation of FNDs in the FND/PCL fibrous matrices with higher FND concentrations (over 0.001 wt% here in Fig. 4c) might result in their reduced tensile Young's modulus [69,70]. The FNDs might restrict the movement of polymer chains, and the dispersion of a larger amount of FNDs would make stronger interaction between FNDs and polymer chains, which would produce a more fragile material [17]. Therefore, 0.001 wt% PCL-FNDs fibrous meshes which revealed improved mechanical properties were selected for further studies.

3.4. Enzymatic degradation

PCL is a polyester, with slow degradation (years) in vitro and in vivo caused by hydrolysis [67]. The degradation path and mechanism has been substantially studied for several decades [50,71,72]. Nonetheless, few researchers paid attention to discover techniques that can assess the extent of degradation by observing inner chain movement in vitro. FNDs have the capability to render the mesh fibres visible in fluorescence microscopy. Further quantum sensing allows real-time monitoring signals during different degradation stages. Incorporating FNDs into PCL scaffolds would provide hints for achieving non-invasive subdermal monitoring. Thus, an accelerated degradation based on enzymatic degradation (PS Lipase) was performed to ascertain the effect of FNDs on the degradation profile of the PCL composite material. Changes in scaffold morphology, mass and fibre diameter as well as crystallinity were collected to show the deformation.

Pure PCL scaffolds were immersed in PS lipase solution as a control group. Single fibre surface morphology and scaffold roughness were observed at a pre-set degradation time by SEM to give further degradation information. Surface roughness increased and filament sizes decreased with degradation time (see Fig. 5a and b). It is worth mentioning that the surface of PCL fibres became rougher sharply after 3 h, and the fibre diameter decreased obviously, as visible on the SEM images (Fig. 5a). Fibre sizes collected in Fig. 5b showed that PCL-FNDs fibres changed moderately, up to 7-day degradation, the fibre diameter decreased by 5 μm whereas there was a 12 μm decrease on PCL fibres. The fibres lost materials caused by the facilitated degradation effect, thus the fibre sizes decreased.

Additionally, for pure PCL, a visible weight loss (Fig. 5d) was seen already after 1 day (over 50%), at day 3 there was around 60%, and at day 7 around 70%. For PCL-FND matrices, less than 40% weight loss was observed after day 1, and at day 7, the weight was around 55%.

PCL with 0.001 wt% nanodiamonds which has higher crystallinity (Fig. 5e) showed better stability during the degradation process. There was not much variation in the degree of crystallinity after 1-week degradation although we observed a slight upward trend of the crystallinity by day 3, that may be caused by reduction of amorphous regions by day 3. Comparatively, the PCL-FNDs group had higher crystallinity at every time point.

Concluding from those results, the PCL-FNDs scaffolds exhibited a significant decrease in degradation rate, which prolonged the usage time of PCL and will extend the usability for long-term applications. Applications such as oral, maxillofacial and the surgical meshes e.g., for spine fusion surgery [73] rely on the long-term stability.

3.5. Fluorescent imaging and T1 measurements

Having FNDs in the material offers the possibility to visualise and, via their NV centers, to monitor the degree of polymer degradation. Fig. 6 shows fluorescent images taken with confocal microscopy. The positions of nanodiamonds are visible as red dots encapsulated in the fibres (shown in blue). As follows, at day 7 (Fig. 6a), we see the breakage of fibres and FNDs agglomeration clearly (circled in Fig. 6a-Day 7). As the degradation time increases, the possibility of nano particle aggregation becomes higher because the cleavage of polymer chains and erosion of inner structure weaken the interaction between nanodiamonds and polymer chains. Due to the intrinsic properties of nano particles, FNDs tend to aggregate and grow into clusters, the clusters would attract more single FND and become larger.

When monitoring the degradation using T1 measurements, FNDs in PCL wires of 1-week degradation delivered the lowest T1 values indicating that the fibre had degraded and that Gd^{3+} was able to come closer to the NV centers (Fig. 6b). From day 1 to day 7, T1 declined continuously which was consistent with the degradation stages under certain erosion treatment time. As mentioned before, after degradation, interconnections between PCL chains and FNDs got weaker and there would be more space inside in comparison to initial PCL fibres which meant Gd^{3+} reached the FNDs easily and the relaxation time decreased. These results demonstrated that the employment of FNDs in bioscaffolds provides a possibility for monitoring real-time polymer degradation.

3.6. Cell viability and proliferation

The biocompatibility of printed scaffolds, containing FNDs was analysed with NHDF-Ad cells.

Fig. 7a–h and i show cell viability and metabolic activity of the cells seeded on both scaffolds with and without FNDs, during one-week of culture. Based on Fig. 7a, cell viability was high in both tested scaffold types, indicating the materials lack of toxicity. Additionally, there was a slight increase observed in the number of cells on PCL-FNDs scaffolds at the first day of culture (Fig. 7b). Growth of cell metabolic activity was

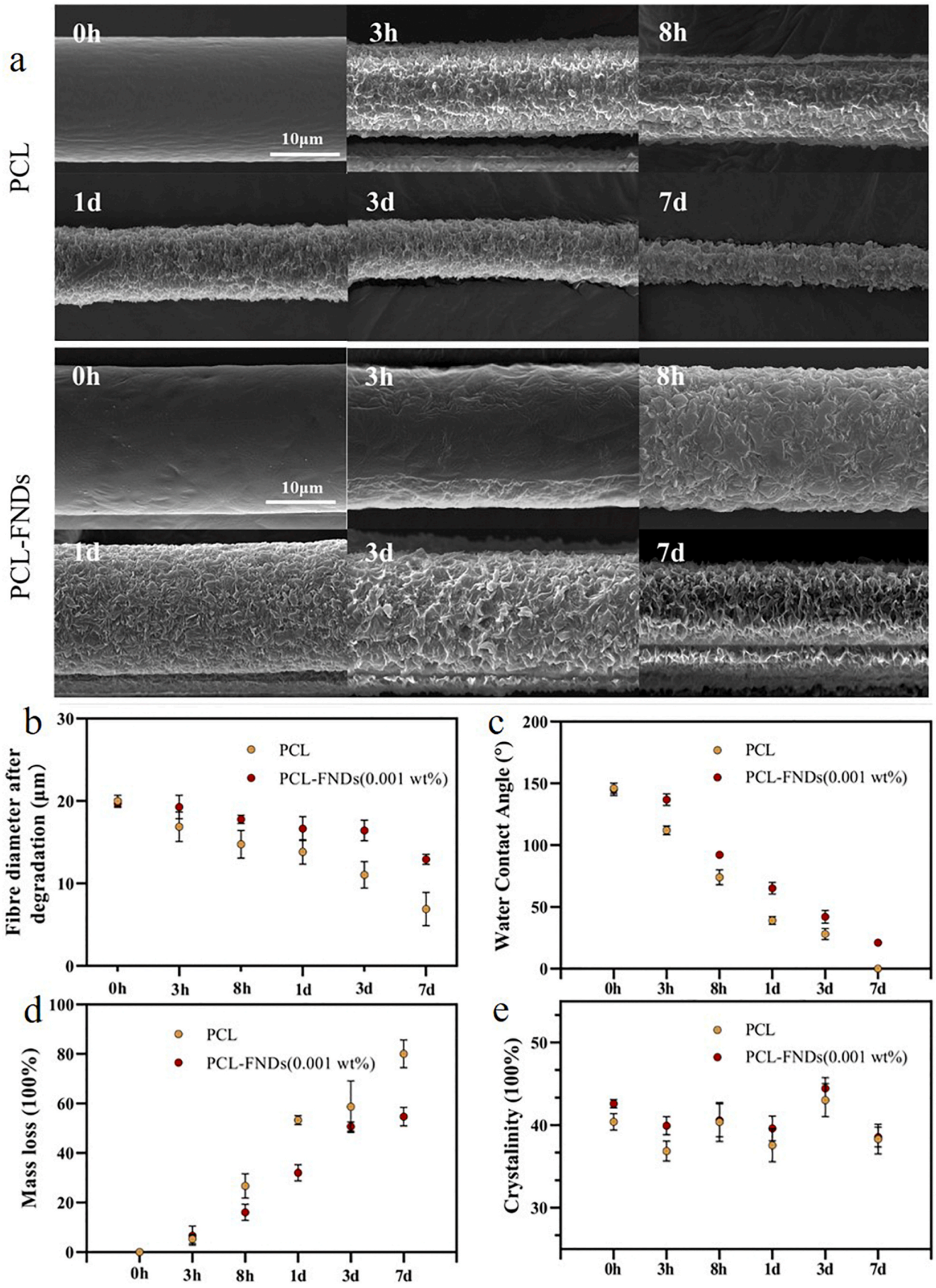

Fig. 5. Degradation studies. a) SEM images showing the fibres incubated in enzymatic solution after 0 h, 3 h, 8 h, 1 day, 3 days and 7 days. b) Fibre diameter. c) Wettability of the scaffolds during 7-days degradation. d) Mass loss of the scaffolds during 7-day enzymatic degradation. e) Crystallinity of scaffolds.

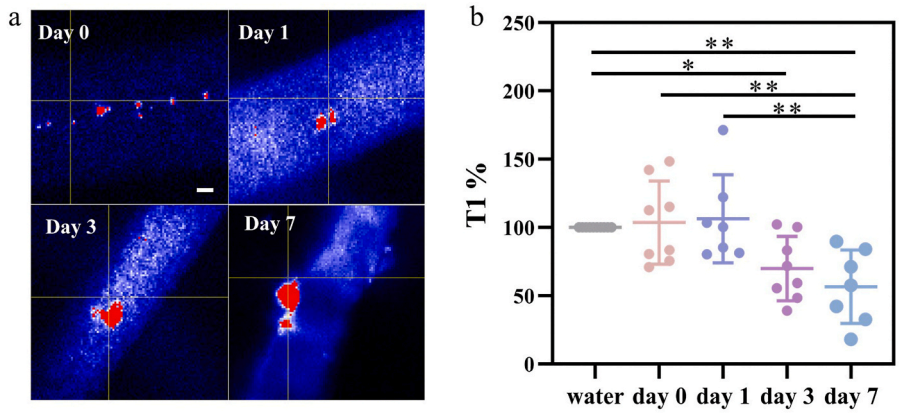

Fig. 6. Use of nanodiamonds to track degradation. a) Fluorescent images of nanodiamonds (0.001 wt%) in PCL fibres after 0-h, 1-day, 3-day and 7-day enzymatic degradation. Scale bar: 3 μm. Nanodiamonds are shown in red, auto fluorescence from fibres is shown in blue. b) T1 relaxation values at set enzymatic degradation time tested in Milli-Q water and 10 μM gadolinium in aqueous solution. 10 particles were measured for each time point. The statistics analysis was described in 2.8. (For interpretation of the references to colour in this figure legend, the reader is referred to the Web version of this article.)

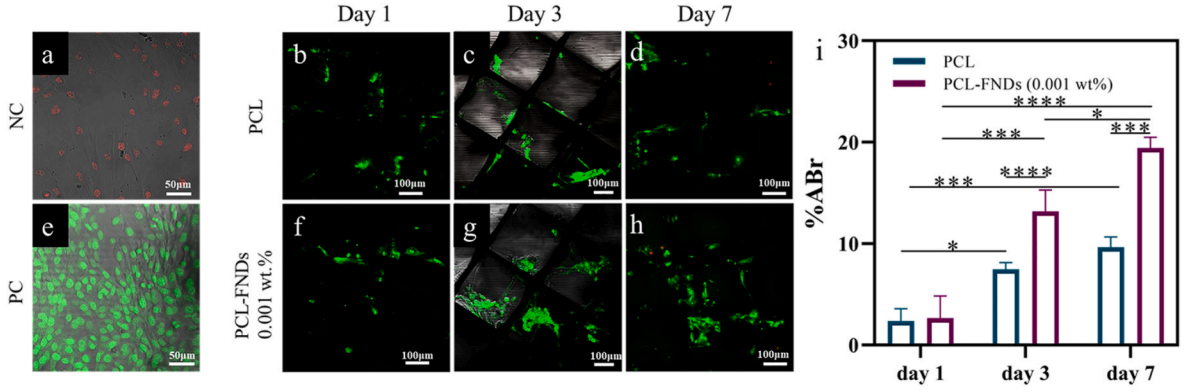

Fig. 7. NHDF-Ad cell behaviour on PCL and PCL-FND (0.001 wt%) scaffolds. a-h) NC and PC were negative control (only dead cells on glass) and positive control (cells on glass), red fluorescence shows dead cells stained by PI and green means that cells were alive and stained by FDA. Cells were viable at day 1, 3 and 7 on both meshes. i) Reduction of AlamarBlue reagent as an indication of cell proliferation rate on the PCL and PCL-FND (0.001 wt%) scaffolds from day 1 to day 7. (For interpretation of the references to colour in this figure legend, the reader is referred to the Web version of this article.)

observed for both scaffold types during 7-day culture. Significantly higher metabolic activity was observed for the scaffolds containing nanodiamonds at day 3 and day 7. This indicated higher cell proliferation of the nanodiamonds-containing scaffolds. Previous studies demonstrated that the hydrophobicity of pure PCL fibres was lowered by adding NDs which enhanced the cell adhesion [38]. Here we did not find variation on hydrophilicity when we introduced FNDs into FNDs into PCL at the low concentration (0.001 wt%) (Fig. 5c. 0 h wettability). However, we assign the improved cell performance to the increased fiber roughness due to the FNDs inclusion. This could encourage the entrapment of fibrin protein [74], and further favour the cell attachment at early stage and proliferation on the PCL mats [75]. Meanwhile, the increased stiffness of the underlying substrates has nonnegligible influence on cell behaviour, which could also improve cell adhesion and proliferation, implying the interaction between cells and scaffold surface microenvironment are beneficial for cell growth [76,77]. Based on the immunofluorescent imaging, no visible differences were observed in morphology of the cells cultured on both types of material (SI Fig. 2).

4. Conclusions

In this paper, PCL scaffolds loaded with FNDs at different concentrations were obtained using MEW. The results demonstrated that addition of FNDs resulted in well-printed PCL scaffolds with 1.25 fold increased tensile modulus, improved thermal and chemical stability, and slower degradation rate, already at a tiny doping concentration of 0.001 wt% FNDs. T1 values of FNDs in fibres after various degradation times provided insight into the degradation stage of the fibres. Additionally, we found that cells adhere and proliferate better on the scaffolds with FNDs addition. In summary PCL-FNDs provides promising avenues for biomedical applications to monitor the tissue response of the polymer and scaffold degradation using a non-invasive detection method.

Funding

This work was supported by China Scholarship Council and The Dutch Research Council (NWO, Veni grant no. VI.Veni.192.148).

CRediT authorship contribution statement

Xixi Wu: Conceptualization, Methodology, Formal analysis, Investigation, Data curation, Writing – original draft, Writing – review & editing. **Thea Vedelaar:** Methodology, Data curation. **Runrun Li:** Methodology. **Romana Schirhagl:** Conceptualization, Methodology, Formal analysis, Writing – review & editing, Supervision, Project administration, Funding acquisition. **Marleen Kamperman:** Methodology, Formal analysis, Writing – review & editing, Supervision, Project administration. **Małgorzata K. Włodarczyk-Biegun:** Methodology, Formal analysis, Writing – review & editing, Supervision, Project administration, Funding acquisition.

Declaration of competing interest

The authors declare the following financial interests/personal relationships which may be considered as potential competing interests:

Malgorzata Wlodarczyk-Biegun reports financial support provided by The Dutch Research Council. Xixi Wu reports financial support provided by China Scholarship Council.

Data availability

Data will be made available on request.

Acknowledgements

X.W. acknowledges the support from China Scholarship Council (CSC), and M.K.W.-B. from The Dutch Research Council (NWO, Veni grant no. VI.Veni.192.148). The Authors thank Mr. Hui Wang for his guidance on taking SEM images.

Appendix A. Supplementary data

Supplementary data to this article can be found online at https://doi.org/10.1016/j.bprint.2023.e00288.

References

[1] A. Eltom, G. Zhong, A. Muhammad, Scaffold Techniques and Designs in Tissue Engineering Functions and Purposes: A Review, 2019, https://doi.org/10.1155/2019/3429527.
[2] V. Guarino, A. Gloria, M.G. Raucci, R. de Santis, L. Ambrosio, Bio-inspired composite and cell instructive platforms for bone regeneration, Int. Mater. Rev. 57 (2012). https://doi.org/10.1179/0950660812Z.00000000021.
[3] É.R. Oliveira, L. Nie, D. Podstawczyk, A. Allahbakhsh, J. Ratnayake, D. Lima Brasil, et al., Molecular Sciences Advances in Growth Factor Delivery for Bone Tissue Engineering, 2021, https://doi.org/10.3390/ijms22020903.
[4] S.J. Hollister, R.D. Maddox, J.M. Taboas, Optimal design and fabrication of scaffolds to mimic tissue properties and satisfy biological constraints, Biomaterials 23 (20) (2002), https://doi.org/10.1016/S0142-9612(02)00148-5.
[5] D.P. Byrne, D. Lacroix, J.A. Planell, D.J. Kelly, P.J. Prendergast, Simulation of tissue differentiation in a scaffold as a function of porosity, Young's modulus and dissolution rate: application of mechanobiological models in tissue engineering, Biomaterials 28 (36) (2007), https://doi.org/10.1016/j.biomaterials.2007.09.003.
[6] S.J. Hollister, Porous scaffold design for tissue engineering, Nat. Mater. 4 (2005). https://doi.org/10.1038/nmat1421.
[7] T.D. Brown, P.D. Dalton, D.W. Hutmacher, Direct writing by way of melt electrospinning, Adv. Mater. 23 (47) (2011), https://doi.org/10.1002/adma.201103482.
[8] N.C. Paxton, M. Lanaro, A. Bo, N. Crooks, M.T. Ross, N. Green, et al., Design tools for patient specific and highly controlled melt electrowritten scaffolds, J. Mech. Behav. Biomed. Mater. 105 (2020), https://doi.org/10.1016/j.jmbbm.2020.103695.
[9] T.M. Robinson, D.W. Hutmacher, P.D. Dalton, The next frontier in melt electrospinning: taming the jet, Adv. Funct. Mater. 29 (2019). https://doi.org/10.1002/adfm.201904664.
[10] M. Gwiazda, S. Kumar, W. Świeszkowski, S. Ivanovski, C. Vaquette, The effect of melt electrospun writing fiber orientation onto cellular organization and mechanical properties for application in Anterior Cruciate Ligament tissue engineering, J. Mech. Behav. Biomed. Mater. 104 (2020), https://doi.org/10.1016/j.jmbbm.2020.103631.
[11] A.M. van Genderen, K. Jansen, M. Kristen, J. van Duijn, Y. Li, C.C.L. Schuurmans, et al., Topographic guidance in melt-electrowritten tubular scaffolds enhances engineered kidney tubule performance, Front. Bioeng. Biotechnol. 8 (2021), https://doi.org/10.3389/fbioe.2020.617364.
[12] A.R. Sadeghi-Avalshahr, S. Nokhasteh, A.M. Molavi, N. Mohammad-Pour, M. Sadeghi, Tailored PCL scaffolds as skin substitutes using sacrificial PVP fibers and collagen/chitosan blends, Int. J. Mol. Sci. 21 (7) (2020), https://doi.org/10.3390/ijms21072311.
[13] S.M. Bittner, B.T. Smith, L. Diaz-Gomez, C.D. Hudgins, A.J. Melchiorri, D.W. Scott, et al., Fabrication and mechanical characterization of 3D printed vertical uniform and gradient scaffolds for bone and osteochondral tissue engineering, Acta Biomater. 90 (2019), https://doi.org/10.1016/j.actbio.2019.03.041.
[14] S. Pok, I.v. Stupin, C. Tsao, R.G. Pautler, Y. Gao, R.M. Nieto, et al., Full-thickness heart repair with an engineered multilayered myocardial patch in rat model, Adv Healthc Mater 6 (5) (2017), https://doi.org/10.1002/adhm.201600549.
[15] M.S. Mohammadi, I. Ahmed, B. Marelli, C. Rudd, M.N. Bureau, S.N. Nazhat, Modulation of polycaprolactone composite properties through incorporation of mixed phosphate glass formulations, Acta Biomater. 6 (8) (2010), https://doi.org/10.1016/j.actbio.2010.03.002.
[16] E. Murray, B.C. Thompson, S. Sayyar, G.G. Wallace, Enzymatic degradation of graphene/polycaprolactone materials for tissue engineering, Polym. Degrad. Stabil. 111 (2015) 71–77, https://doi.org/10.1016/j.polymdegradstab.2014.10.010. Elsevier Ltd.
[17] J.H.Y. Chung, S. Sayyar, G.G. Wallace, Effect of graphene addition on polycaprolactone scaffolds fabricated using melt-electrowriting. Polymers (basel), MD 14 (2) (2022), https://doi.org/10.3390/polym14020319.
[18] S. Shahmoradi, F. Yazdian, F. Tabandeh, Z.S. Soheili, A.S. Hatamian Zarami, M. Navaei-Nigjeh, Controlled surface morphology and hydrophilicity of polycaprolactone toward human retinal pigment epithelium cells, Mater. Sci. Eng. C 73 (2017), https://doi.org/10.1016/j.msec.2016.11.076.
[19] Y. Hou, W. Wang, P. Bártolo, Investigating the effect of carbon nanomaterials reinforcing poly(ε-Caprolactone) printed scaffolds for bone repair applications, Int J Bioprint 6 (2) (2020), https://doi.org/10.18063/ijb.v6i2.266.
[20] J.B. Vella, R.P. Trombetta, M.D. Hoffman, J. Inzana, H. Awad, D.S.W. Benoit, Three dimensional printed calcium phosphate and poly(caprolactone) composites with improved mechanical properties and preserved microstructure, J. Biomed. Mater. Res. 106 (3) (2018), https://doi.org/10.1002/jbm.a.36270.
[21] R. Trombetta, J.A. Inzana, E.M. Schwarz, S.L. Kates, H.A. Awad, 3D printing of calcium phosphate ceramics for bone tissue engineering and drug delivery, Ann. Biomed. Eng. 45 (1) (2017), https://doi.org/10.1007/s10439-016-1678-3.
[22] K. Fox, R. Ratwatte, M.A. Booth, H.M. Tran, P.A. Tran, High nanodiamond content-PCL composite for tissue engineering scaffolds, Nanomaterials. MDPI AG 10 (5) (2020), https://doi.org/10.3390/nano10050948.
[23] S. Houshyar, G.S. Kumar, A. Rifai, N. Tran, R. Nayak, R.A. Shanks, et al., Nanodiamond/poly-ε-caprolactone nanofibrous scaffold for wound management, Mater. Sci. Eng. C 100 (2019) 378–387, https://doi.org/10.1016/j.msec.2019.02.110. Elsevier Ltd.
[24] Zhijun Chen, Yljhmhxhxqjfhyby, Influences of process parameters of near-field direct-writing melt electrospinning on performances of polycaprolactone/nano-hydroxyapatite scaffolds, Polymer 14 (6) (2022), 3404, https://doi.org/10.3390/polym14163404.
[25] E. Hewitt, S. Mros, M. McConnell, J.D. Cabral, A. Ali, Melt-electrowriting with novel milk protein/PCL biomaterials for skin regeneration, Biomed. Mater. 14 (5) (2019), https://doi.org/10.1088/1748-605X/ab3344.
[26] A.M. Schrand, S.A.C. Hens, O.A. Shenderova, Nanodiamond particles: properties and perspectives for bioapplications, Crit. Rev. Solid State Mater. Sci. 34 (1 2) (2009), https://doi.org/10.1080/10408430902831987.
[27] V. Vaijayanthimala, H.C. Chang, Functionalized fluorescent nanodiamonds for biomedical applications, Nanomedicine 4 (2009). https://doi.org/10.2217/17435889.4.1.47.
[28] A. Nagl, S.R. Hemelaar, R. Schirhagl, Improving surface and defect center chemistry of fluorescent nanodiamonds for imaging purposes-a review, Anal. Bioanal. Chem. 407 (2015). https://doi.org/10.1007/s00216-015-8849-1.
[29] F. Jelezko, J. Wrachtrup, Single defect centres in diamond: a review, Phys. Status Solidi A 203 (2006). https://doi.org/10.1002/pssa.200671403.
[30] P. Kehayias, M.W. Doherty, D. English, R. Fischer, A. Jarmola, K. Jensen, et al., Infrared absorption band and vibronic structure of the nitrogen-vacancy center in diamond, Phys. Rev. B Condens. Matter 88 (16) (2013), https://doi.org/10.1103/PhysRevB.88.165202.
[31] Y. Wu, F. Jelezko, M.B. Plenio, T. Weil, Diamond Quantum Devices in Biology, Angewandte Chemie - International Edition (2016). https://doi.org/10.1002/anie.201506556.
[32] S. Hong, M.S. Grinolds, L.M. Pham, D. le Sage, L. Luan, R.L. Walsworth, et al., Nanoscale Magnetometry with NV Centers in Diamond, 38, MRS Bulletin, 2013. https://doi.org/10.1557/mrs.2013.23.
[33] A. Gruber, A. Dräbenstedt, C. Tietz, L. Fleury, J. Wrachtrup, C. von Borczyskowski, Scanning confocal optical microscopy and magnetic resonance on single defect centers, Science 276 (5321) (1979), https://doi.org/10.1126/science.276.5321.2012, 1997.
[34] K. Fox, P.A. Tran, D.W.M. Lau, T. Ohshima, A.D. Greentree, B.C. Gibson, Nanodiamond-polycaprolactone composite: a new material for tissue engineering with sub-dermal imaging capabilities, Mater Lett. Elsevier 185 (2016) 185–188, https://doi.org/10.1016/j.matlet.2016.08.140.
[35] K. Fox, R. Ratwatte, M.A. Booth, H.M. Tran, P.A. Tran, High nanodiamond content-PCL composite for tissue engineering scaffolds, Nanomaterials. MDPI AG 10 (5) (2020), https://doi.org/10.3390/nano10050948.
[36] A. Rifai, S. Houshyar, K. Fox, Progress towards 3D-printing diamond for medical implants: a review, Annals of 3D Printed Medicine 1 (2021), 100002, https://doi.org/10.1016/j.stlm.2020.100002. Elsevier BV.
[37] G.Y. Ahn, T.K. Ryu, Y.R. Choi, J.R. Park, M.J. Lee, S.W. Choi, Fabrication and optimization of Nanodiamonds-composited poly(ε-caprolactone) fibrous matrices for potential regeneration of hard tissues, Biomater Res. BioMed Central Ltd. 22 (1) (2018), https://doi.org/10.1186/s40824-018-0126-x.
[38] S. Houshyar, G.S. Kumar, A. Rifai, N. Tran, R. Nayak, R.A. Shanks, et al., Nanodiamond/poly-ε-caprolactone nanofibrous scaffold for wound management, Mater. Sci. Eng. C 100 (2019) 378–387, https://doi.org/10.1016/j.msec.2019.02.110. Elsevier Ltd.
[39] K. Wu, T.A. Vedelaar, V.G. Damle, A. Morita, J. Mougnaud, C. Reyes San Martin, et al., Applying NV center-based quantum sensing to study intracellular free radical response upon viral infections, Redox Biol. 52 (2022), https://doi.org/10.1016/j.redox.2022.102279.
[40] R. Sakaguchi, S. Kiyonaka, Y. Mori, Fluorescent sensors reveal subcellular thermal changes, Curr. Opin. Biotechnol. 31 (2015). https://doi.org/10.1016/j.copbio.2014.07.013.
[41] E. Glushkov, V. Navikas, A. Radenovic, Fluorescent nanodiamonds as versatile intracellular temperature sensors, Chimia 73 (1 2) (2019), https://doi.org/10.2533/chimia.2019.73.
[42] R. Sharmin, T. Hamoh, A. Sigaeva, A. Mzyk, V.G. Damle, A. Morita, et al., Fluorescent nanodiamonds for detecting free-radical generation in real time during

shear stress in human umbilical vein endothelial cells, ACS Sens. 6 (12) (2021), https://doi.org/10.1021/acssensors.1c01582.
[43] L. Nie, A.C. Nusantara, V.G. Damle, R. Sharmin, E.P.P. Evans, S.R. Hemelaar, et al., Quantum monitoring of cellular metabolic activities in single mitochondria, Sci. Adv. 7 (21) (2021), https://doi.org/10.1126/sciadv.abf0573.
[44] N. Norouzi, A.C. Nusantara, Y. Ong, T. Hamoh, L. Nie, A. Morita, et al., Relaxometry for detecting free radical generation during Bacteria's response to antibiotics, Carbon N Y. Pergamon 199 (2022) 444–452, https://doi.org/10.1016/J.CARBON.2022.08.025.
[45] O.A. Shenderova, A.I. Shames, N.A. Nunn, M.D. Torelli, I. Vlasov, A. Zaitsev, Review Article: synthesis, properties, and applications of fluorescent diamond particles, J. Vac. Sci. Technol. B 37 (3) (2019), https://doi.org/10.1116/1.5089898.
[46] S.Y. Ong, R.J.J. van Harmelen, N. Norouzi, F. Offens, I.M. Venema, M.B. Habibi Najafi, et al., Interaction of nanodiamonds with bacteria, Nanoscale 10 (36) (2018), https://doi.org/10.1039/c8nr05183f.
[47] J. Kong, Y. Yu, X.P. Pei, C. Han, Y. Tan, L. Dong, Polycaprolactone nanocomposite reinforced by bioresource starch-based nanoparticles, Int J Biol Macromol. Elsevier 102 (2017) 1304, https://doi.org/10.1016/J.IJBIOMAC.2017.05.019, 11.
[48] Ju D, Han L, Li F, Chen S, Dong L. Crystallization, Mechanical Properties, and Enzymatic Degradation of Biodegradable Poly(e-Caprolactone) Composites with Poly(lactic Acid) Fibers. DOI: 10.1002/pc.22578.
[49] G. Hochleitner, E. Fürsattel, R. Giesa, J. Groll, H.W. Schmidt, P.D. Dalton, Melt electrowriting of thermoplastic elastomers, Macromol. Rapid Commun. 39 (10) (2018), https://doi.org/10.1002/marc.201800055.
[50] M. Bartnikowski, T.R. Dargaville, S. Ivanovski, D.W. Hutmacher, Degradation mechanisms of polycaprolactone in the context of chemistry, geometry and environment, Prog. Polym. Sci. 96 (2019). https://doi.org/10.1016/j.progpolymsci.2019.05.00.
[51] A. Morita, T. Hamoh, F.P. Perona Martinez, M. Chipaux, A. Sigaeva, C. Mignon, et al., The fate of lipid-coated and uncoated fluorescent nanodiamonds during cell division in yeast, Nanomaterials 10 (3) (2020), https://doi.org/10.3390/nano10030516.
[52] F. Perona Martínez, A.C. Nusantara, M. Chipaux, S.K. Padamati, R. Schirhagl, Nanodiamond relaxometry-based detection of free-radical species when produced in chemical reactions in biologically relevant conditions, ACS Sens. 5 (12) (2020), https://doi.org/10.1021/acssensors.0c01037.
[53] A. Morita, T. Hamoh, F.P. Perona Martinez, M. Chipaux, A. Sigaeva, C. Mignon, et al., The fate of lipid-coated and uncoated fluorescent nanodiamonds during cell division in yeast, Nanomaterials 10 (3) (2020), https://doi.org/10.3390/nano10030516.
[54] R. Li, T. Vedelaar, A. Mzyk, A. Morita, S.K. Padamati, R. Schirhagl, Following polymer degradation with nanodiamond magnetometry, ACS Sens. 7 (1) (2022), https://doi.org/10.1021/acssensors.1c01782.
[55] F. Perona Martínez, A.C. Nusantara, M. Chipaux, S.K. Padamati, R. Schirhagl, Nanodiamond relaxometry-based detection of free-radical species when produced in chemical reactions in biologically relevant conditions, ACS Sens. 5 (12) (2020), https://doi.org/10.1021/acssensors.0c01037.
[56] M.A. Zachari, P.S. Chondrou, S.E. Pouliliou, A.G. Mitrakas, I. Abatzoglou, C.E. Zois, et al., Evaluation of the alamarblue assay for adherent cell irradiation experiments, Formerly Nonlinearity in Biology 12 (2014) 246, https://doi.org/10.2203/dose-response.13-024.Koukourakis, 58.
[57] Y.W. Chen, C.H. Lee, Y.L. Wang, T.L. Li, H.C. Chang, Nanodiamonds as nucleating agents for protein crystallization, Langmuir 33 (26) (2017), https://doi.org/10.1021/acs.langmuir.7b00578.
[58] Q.L. Loh, C. Choong, Three-dimensional scaffolds for tissue engineering applications: role of porosity and pore size, Tissue Eng. B Rev. 19 (2013). https://doi.org/10.1089/ten.teb.2012.0437.
[59] S.J. Hollister, Porous scaffold design for tissue engineering, Nat. Mater. 4 (2005). https://doi.org/10.1038/nmat1421.
[60] N. Schaefer, D. Janzen, E. Bakirci, A. Hrynevich, P.D. Dalton, C. Villmann, 3D electrophysiological measurements on cells embedded within fiber-reinforced matrigel, Adv Healthc Mater 8 (5) (2019), https://doi.org/10.1002/adhm.201801226.
[61] J van Turnhout, Thermally stimulated discharge of polymer electrets, Polym. J. 2 (2) (1971), https://doi.org/10.1295/polymj.2.173.
[62] K. Cao, F. Zhang, A. Zaeri, R. Zgeib, R.C. Chang, Quantitative investigation into the design and process parametric effects on the fiber-entrapped residual charge for a polymer melt electrohydrodynamic printing process, Macromol. Mater. Eng. 307 (3) (2022 Mar), 2100766. https://doi.org/10.1002/mame.202100766.
[63] S.R. Holmes-Farley, C.D. Bain, G.M. Whitesides, Wetting of functionalized polyethylene film having ionizable organic acids and bases at the polymer-water interface: relations between functional group polarity, extent of ionization, and contact angle with water, Langmuir 4 (4) (1988), https://doi.org/10.1021/la00082a025.
[64] L. Zhu, Q. Wang, Novel ferroelectric polymers for high energy density and low loss dielectrics, Macromolecules 45 (2012). https://doi.org/10.1021/ma2024057.
[65] A.L. Yarin, S. Koombhongse, D.H. Reneker, Bending instability in electrospinning of nanofibers, J. Appl. Phys. 89 (5) (2001), https://doi.org/10.1063/1.1333035.
[66] M.M. Hohman, M. Shin, G. Rutledge, Electrospinning and electrically forced jets. I. Stability theory, Phys. Fluids 13 (2001) 2201, https://doi.org/10.1063/1.1383791.
[67] M. Bartnikowski, T.R. Dargaville, S. Ivanovski, D.W. Hutmacher, Degradation mechanisms of polycaprolactone in the context of chemistry, geometry and environment, Prog. Polym. Sci. 96 (2019 Sep 1) 1–20.
[68] U. Maitra, K.E. Prasad, U. Ramamurty, C.N. Rao, Mechanical properties of nanodiamond-reinforced polymer-matrix composites, Solid State Commun. 149 (39–40) (2009 Oct 1) 1693–1697. https://doi.org/10.1016/j.progpolymsci.2019.05.004.
[69] Z. Wang, N. Cai, D. Zhao, J. Xu, Q. Dai, Y. Xue, et al., Mechanical Reinforcement of Electrospun Water-Soluble Polymer Nanofibers Using Nanodiamonds, 2013, https://doi.org/10.1002/pc.22577.
[70] N. Cai, Q. Dai, Z. Wang, X. Luo, Y. Xue, F. Yu, Preparation and properties of nanodiamond/poly(lactic acid) composite nanofiber scaffolds, Fibers Polym. 15 (12) (2014) 2544, https://doi.org/10.1007/s12221-014-2544-2, 52.
[71] R.M. Mohamed, K. Yusoh, A review on the recent research of polycaprolactone (PCL), Adv. Mater. Res. 1134 (2015). https://doi.org/10.4028/www.scientific.net/amr.1134.249. https://doi.org/10.3390/polym11040651.
[72] R. Scaffaro, A. Maio, F. Sutera, Gulino E. ortunato, M. Morreale, Degradation and recycling of films based on biodegradable polymers: a short review, Polymers 11 (2019). https://doi.org/10.3390/polym11040651.
[73] P.K. Yarlagadda, M. Chandrasekharan, J.Y. Shyan, Recent advances and current developments in tissue scaffolding, Bio Med. Mater. Eng. 15 (3) (2005 Jan 1) 159–177.
[74] Zareidoost A, Yousefpour M, Ghaseme B, Amanzadeh A. The Relationship of Surface Roughness and Cell Response of Chemical Surface Modification of Titanium. DOI: 10.1007/s10856-012-4611-9.
[75] H.H. Kim, M.J. Kim, S.J. Ryu, C.S. Ki, Y.H. Park, Effect of fiber diameter on surface morphology, mechanical property, and cell behavior of electrospun poly (ε-caprolactone) mat, Fibers Polym. 17 (7) (2016) 1033, https://doi.org/10.1007/s12221-016-6350-x, 42.
[76] B.A.C. Harley, H do Kim, M.H. Zaman, I.v. Yannas, D.A. Lauffenburger, L.J. Gibson, Microarchitecture of three-dimensional scaffolds influences cell migration behavior via junction interactions, Biophys. J. 95 (8) (2008), https://doi.org/10.1529/biophysj.107.122598.
[77] K.M. Kennedy, A. Bhaw-Luximon, D. Jhurry, Cell-matrix mechanical interaction in electrospun polymeric scaffolds for tissue engineering: implications for scaffold design and performance, Acta Biomater 50 (2017). https://doi.org/10.1016/j.actbio.2016.12.034.